AIAA 2002-0156
Time-accurate Simulations of Hypersonic Boundary Layer Stability and Transition over Blunt Bodies Using Implicit Parallel Algorithms

Haibo Dong and Xiaolin Zhong
University of California, Los Angeles
Los Angeles, CA

40th Aerospace Sciences Meeting & Exhibit
January 14–17, 2002 / Reno, NV

Time-accurate Simulations of Hypersonic Boundary Layer Stability and Transition over Blunt Bodies Using Implicit Parallel Algorithms

Haibo Dong *and Xiaolin Zhong †
University of California, Los Angeles, California 90095

Abstract

The receptivity process of hypersonic boundary layer flows over blunt leading edges has been paid more attentions in recent years. After free stream disturbances pass through and interact with the bow shock, three kinds of transmitted waves will be generated and interact with the boundary layer on the body during propagation to downstream. This generated complex wave field behind the bow shock will lead linear eigenmode growth or transient growth of perturbations inside boundary layer. Due to the progress of computer techniques, Direct numerical simulation (DNS) has recently become a powerful tool to study the stability and transition of compressible boundary layers. 3-D unsteady Navier-Stokes equations are numerically simulated without using any empirical turbulence models. Highly efficient and accurate numerical methods are implemented in the numerical simulation of such complicated problems. In this paper, we extend our previous work to do the direct numerical simulation of hypersonic boundary layer stability and transition over blunt bodies by using high-order parallel time-accurate semi-implicit shock-fitting and Fourier spectral code on massively distributed memory computers. Meanwhile, Linear stability theory (LST) is used to do the analysis on the base mean flow. Our numerical methods has been firstly validated by comparing numerical results with experimental results and results predicted by LST. Then, detailed numerical simulations of 3-D hypersonic boundary layer receptivity to fast acoustic waves and vorticity waves have been investigated. On-going work of investigating transient growth of 3-D perturbations in viscous hypersonic boundary layer over blunt wedge is in progress.

1 Introduction

The prediction of laminar-turbulent transition in hypersonic boundary layers is a critical part of the aerodynamic design and control of hypersonic vehicles. The transition process is a result of nonlinear response of laminar boundary layers to forcing disturbances [1,2], which can originate from many difference sources including free stream disturbances, surface roughness and vibrations [3]. In an environment with weak initial disturbances, the path to transition consists of three stages: 1) receptivity, 2) linear eigenmode growth or transient growth, and 3) nonlinear breakdown to turbulence.

The first stage is the receptivity process [4], which converts the environmental disturbances into initial instability waves in the boundary layers. Theoretical results on incompressible boundary layer receptivity are mainly obtained based on the asymptotic theory [5,6]. The asymptotic analysis explains how the long wavelength free stream acoustic disturbances enter the boundary layer and generate short-wavelength Tollmien-Schlichting (T-S) waves in incompressible boundary layers. The receptivity mechanism provides important initial conditions of amplitude, frequency, and phase of instability waves in the boundary layers. The direct numerical simulation, which numerically solves the full Navier-Stokes equations as an initial-boundary problem, has become an important tool in receptivity and transition studies in recent years. The direct numerical simulation of the receptivity of incompressible boundary layers has been performed by Murdock [7]; Lin, Reed, and Saric [8]; Buter and Reed [9]; and Collis and Lele [10].

The stability and transition of supersonic and hypersonic boundary layers was reviewed by Mack [11], Morkovin [12], Arnal [13], and Reed and Saric [14]. The receptivity process of hypersonic boundary layer flows over blunt leading edges has been paid more attentions in recent years. For hypersonic boundary-layer flows over blunt bodies, the receptivity phenomena are much more complex and are currently not well understood [12,15]. Figure 1 shows a schematic of wave interactions in the leading edge region of a hypersonic flow in the presence of free stream disturbances. The receptivity phenomena are altered considerably by the bow shock in front of the body. The interaction of free stream waves with the shock affects the receptivity process of the boundary layer behind the shock. Kovasznay [16] showed that weak disturbance waves in compressible flow can be decomposed into three independent modes: acoustic, entropy, and vorticity modes. The acoustic wave is propagated with the speed of sound

*Ph.D. Student, Mechanical and Aerospace Engineering Department, Student Member AIAA, haibo@seas.ucla.edu
†Associate Professor, Mechanical and Aerospace Engineering Department, Associate Fellow AIAA, xiaolin@seas.ucla.edu.

relative to the moving fluid, while the entropy and vorticity waves convect with the moving fluid velocity. Before entering the boundary layer, free stream disturbances first pass through and interact with the bow shock. Irrespective of the nature of a free stream disturbance wave, its interaction with the bow shock always generates all three types of disturbance waves [17] after passing through the shock. These three kinds of transmitted waves are propagated downstream and interact with the boundary layer on the body. At the same time, the perturbed boundary layer also generates reflected acoustic wave propagating upstream. When it reaches back to impinge on the shock from behind, the reflected acoustic wave generates at the shock additional three kinds of disturbances which also propagate down stream. Such back and forth reflection and interaction creates a complex wave field behind the bow shock. The combined effects of these interactions determine the receptivity process of the hypersonic boundary layer behind the shock.

The second stage is the subsequent linear development and growth of boundary-layer instability waves. Relevant instability waves for hypersonic boundary layers include the first mode and higher mode instability [11], the Görtler instability over concave surfaces [18], attachment line instability in leading edges, and cross flow instability in three-dimensional boundary layers [14]. Another possible second stage of the transition process is transient growth mechanism. Transient growth [19–25] arises through the nonorthogonal nature of the Orr-Sommerfeld and Squire eigenfunctions. According to Ref. [25], the largest effect comes from the nonorthogonal superposition of slightly damped, highly oblique (near streamwise) T-S and Squire modes. Transient growth is considered as a candidate mechanism for many examples of bypass transition. Many research has been done in this field. The study of transient growth emanated from Landahl [19]'s "lift-up" mechanism, a localized three-dimensional updown motion in regions of high mean shear (near the wall) that grows algebraically in time. Butler and Farrell [20] determined optimal disturbance parameters for maximum transient growth in plane Couette, plane Poiseuille, and Blasius flows. Consideration of transient growth has lead to an enlargement and clarification of the paths to transition by Morkovin, Reshotko, and Herbert [26]. Upon on their clarification, there are five possible paths to transition. Among those paths, some transient growth may provide a higher amplitude to the eigenmode growth upon crossing into an exponentially unstable region. If the transition growth is large enough, it could directly excite secondary instabilities and mode interactions. Spatial theories of linear transient growth for disturbances in a circular pine [24] and in a parallel boundary layer [27] have been presented recently. It is shown that stationary disturbances may achieve more significant transient growth than nonstationary ones. Numerical examples illustrate that favorable pressure gradient decreases the overall amplification. Reshotko [25] recently analytically studied the problem of the "blunt body paradox", which refers to the early transition on speeds both in flight and in wind tunnels. This transition occurs usually in the subsonic portion of the flow behind the bow shock wave, a region of highly favorable pressure gradient that is stable to T-S waves, even the surface is smooth. Meanwhile, surface cooling leads to even earlier transition. The tentative suggestions are generally roughness related since stagnation point boundary layers are very thin. But no connection has been made between the microscopic roughness on the surface and the features of the observed early transition such as location, sensitivity to surface temperature level, etc. This has led to a search for an explanation through transient growth.

The objective of this paper is to extend the previous 2-D and 3-D parallel high-order shock-fitting schemes in [28–30] to solve compressible Navier-Stokes equations implicitly on massively distributed memory computers. Divide and conquer algorithm are used to solved the big banded Jacobian matrices from implicit methods. Meanwhile, Linear stability theory (LST) is used to do the theoretical analysis. Our numerical methods has been firstly validated by comparing numerical results with experimental results and results predicted by LST. Then, detailed numerical simulations of 3-D hypersonic boundary layer receptivities to fast acoustic waves and vorticity waves have been investigated. On-going work of investigating transient growth of 3-D perturbations in viscous hypersonic boundary layer over blunt wedge is in progress.

2 Governing Equations and Numerical Methods

2.1 Governing Equations

The governing equations are the unsteady three-dimensional Navier-Stokes equations written in a conservation-law form

$$\frac{\partial U}{\partial t} + \frac{\partial F_j}{\partial x_j} + \frac{\partial F_{vj}}{\partial x_j} = 0 \tag{1}$$

where

$$U = \{\rho,\ \rho u_1,\ \rho u_2,\ \rho u_3,\ e\} \tag{2}$$

$$F_j = \begin{Bmatrix} \rho u_j \\ \rho u_1 u_j + p\delta_{1j} \\ \rho u_2 u_j + p\delta_{2j} \\ \rho u_3 u_j + p\delta_{3j} \\ (e+p)\,u_j \end{Bmatrix} \tag{3}$$

$$F_{vj} = \begin{Bmatrix} 0 \\ \tau_{1j} \\ \tau_{2j} \\ \tau_{3j} \\ \tau_{jk}u_k - q_j \end{Bmatrix} \tag{4}$$

$$p = \rho RT \quad (5)$$

$$e = \rho(c_v T + \frac{\rho}{2} u_k u_k) \quad (6)$$

$$\tau_{ij} = -\mu\left(\frac{\partial u_i}{\partial x_j} + \frac{\partial u_j}{\partial x_i}\right) + 2\mu/3\frac{\partial u_k}{\partial x_k}\delta_{ij} \quad (7)$$

$$q_j = -\kappa\frac{\partial T}{\partial x_j} \quad (8)$$

The details for the expressions above can be found in [31]. The viscosity and heat conductivity coefficients are computed by the Sutherland law and the assumption of a constant Prandtl number. Perfect gas assumption is used in all flows considered in this paper, though the method presented here can be easily extended to nonequilibrium real-gas hypersonic flows.

For numerical simulations of flow fields over a curved body surface, structured body fitted grids are used to transform the governing equations (1) in the Cartesian coordinates into a set of curvilinear three-dimensional coordinates (ξ, η, ζ, τ) along the body fitted grid lines. The transformation relations for the two set of coordinates are

$$\begin{cases} \xi = \xi(x,y,z,t) \\ \eta = \eta(x,y,z,t) \\ \zeta = \zeta(x,y,z,t) \\ \tau = t \end{cases} \Longleftrightarrow \begin{cases} x = x(\xi,\eta,\zeta,\tau) \\ y = y(\xi,\eta,\zeta,\tau) \\ y = y(\xi,\eta,\zeta,\tau) \\ t = \tau \end{cases} \quad (9)$$

The governing equations (1) are transformed as follows

$$\frac{1}{J}\frac{\partial U}{\partial \tau} + \frac{\partial E'}{\partial \xi} + \frac{\partial F'}{\partial \eta} + \frac{\partial G'}{\partial \zeta} + \frac{\partial E'_v}{\partial \xi} + \frac{\partial F'_v}{\partial \eta} + \frac{\partial G'_v}{\partial \zeta} + U\frac{\partial(\frac{1}{J})}{\partial \tau} = 0 \quad (10)$$

where

$$E' = \frac{F_1\xi_x + F_2\xi_y + F_3\xi_z + U\xi_t}{J} \quad (11)$$

$$F' = \frac{F_1\eta_x + F_2\eta_y + F_3\eta_z + U\eta_t}{J} \quad (12)$$

$$G' = \frac{F_1\zeta_x + F_2\zeta_y + F_3\zeta_z + U\zeta_t}{J} \quad (13)$$

$$E'_v = \frac{F_{v1}\xi_x + F_{v2}\xi_y + F_{v3}\xi_z}{J} \quad (14)$$

$$F'_v = \frac{F_{v1}\eta_x + F_{v2}\eta_y + F_{v3}\eta_z}{J} \quad (15)$$

$$G'_v = \frac{F_{v1}\zeta_x + F_{v2}\zeta_y + F_{v3}\zeta_z}{J} \quad (16)$$

where J is the Jacobian of the coordinate transformation, and ξ_x, ξ_y, ξ_z, η_x, η_y, η_z, η_t, ζ_x, ζ_y, and ζ_z are the grid transformation matrices. In the equations, the transformed inviscid fluxes E', F', and G' are standard flux terms with known eigenvalues and eigenvectors. The transport flux terms E'_v, F'_v, and G'_v contain both first-order and second-order spatial derivatives of velocity and temperature. These derivatives in the Cartesian coordinates (x, y, z) are transformed into the computational coordinates (ξ, η, ζ) using a chain rule for spatial discretization.

2.2 Numerical Methods

2.2.1 High-Order Semi-Implicit Method

The stiffness of viscous flow simulations is mainly due to terms associated with derivatives in the wall-normal direction ($\frac{\partial()}{\partial\eta}$ and $\frac{\partial^2()}{\partial\eta^2}$) because of grid stretching near the wall. Therefore, Navier-Stocks Equation (10) for a three-dimensional flow in (ξ, η, ζ, τ) is additively split into relatively nonstiff part $\mathbf{f}(U_{ijk})$ and stiff part $\mathbf{g}(U_{ijk})$ as follows

$$\frac{1}{J}\frac{\partial U_{ijk}}{\partial t} = \mathbf{f}(U_{ijk}) + \mathbf{g}(U_{ijk}) \quad (17)$$

where details can be found in Ref. [30]. In Eq. (17), $\mathbf{g}(U_{ijk})$ is much stiffer than $\mathbf{f}(U_{ijk})$ since grid spacing in the wall-normal direction is much smaller than that used in streamwise direction for most viscous flow simulations. Therefore, high-order semi-implicit method can be used to overcome the stiffness of $\mathbf{g}(U_{ijk})$ while maintaining high-order temporal accuracy.

The split governing equation (17) is first approximated by high-order accurate finite difference methods. For the case of direct numerical simulation of compressible boundary layers with a bow shock, the shock wave can be treated by a shock-fitting method because there is no discontinuity in the interior of the computational domain. In this paper, a fifth-order upwind scheme [28] is used to discretize the inviscid flux derivatives. Meanwhile, high-order central difference schemes, such as the sixth-order central scheme, are used to discretize the viscous flux terms in the equations. A simple local Lax-Friedrichs scheme is used to split the inviscid flux vectors into positive and negative wave fields. Details of derivations can be found in Ref. [30]. The spatial discretization of the split Eq. (17) using these high-order schemes coupled with appropriate boundary conditions leads to a system of ordinary differential equations in the form of

$$\frac{d\mathbf{u}}{dt} = [\mathbf{f}(t,\mathbf{u})] + [\mathbf{g}(t,\mathbf{u})] \quad (18)$$

where $\mathbf{u} = \{U_{ij}, \text{for } i = 1,\cdots IL,\ j = 1,\cdots JL\}$ is the vector of all discretized variables in the flow field, $[\mathbf{f}(t,\mathbf{u})]$ represents the discretized nonstiff term, and $[\mathbf{g}(t,\mathbf{u})]$ represents the discretized stiff term.

The system of ordinary differential equations of Eq. (17) can be integrated in time using semi-implicit temporal schemes, where $\mathbf{f}$ is treated explicitly and $\mathbf{g}$ is treated implicitly. It was shown by Zhong [32] that in order to have a third or higher order temporal accuracy, the semi-implicit method need to be derived in a way that the effects of coupling between the implicit and explicit terms on the accuracy need be considered. Zhong [32] subsequently derived three kinds of third-order semi-implicit Runge-Kutta schemes for high-order temporal integration of the governing equations for reacting flow simulations. High-order low-storage semi-implicit Runge-Kutta method versions(LSSIRK) have

also been derived in [33]. In particular, Rosenbrock type Runge-Kutta (LSSIRK-rC) Method can be written as following

$$\begin{cases} [\mathbf{I} - hc_j\mathbf{J}(\mathbf{u}_{j-1} + \bar{c}_j\mathbf{k}_{j-1})]\,\mathbf{k}_j = \\ \qquad h\left(\mathbf{f}(\mathbf{u}_{j-1}) + \mathbf{g}(\mathbf{u}_{j-1} + \bar{c}_j\mathbf{k}_{j-1})\right) \\ \qquad + a_j\,[\mathbf{I} - hc_j\mathbf{J}(\mathbf{u}_{j-1} + \bar{c}_j\mathbf{k}_{j-1})]\,\mathbf{k}_{j-1} \\ \mathbf{u}_j = \mathbf{u}_{j-1} + b_j\mathbf{k}_j \end{cases} \tag{19}$$

where $j = 1, ..., r$ and parameters c_j, $\bar{c}_j$, b_j can be found in [33]. For instance, in LSSIRK-3C, $b_1 = \frac{1}{4}$, $b_2 = \frac{2}{9}$, $b_3 = 3$, $a_1 = -\frac{1}{4}$, $a_2 = -\frac{29}{27}$, $c_1 = 2.26760$, $c_2 = 2.68530$, $c_3 = 2.30975$, $\bar{c}_2 = -1.14310$, and $\bar{c}_3 = -2.03122$. The parameters of the semi-implicit Runge-Kutta methods are chosen by both stability and accuracy requirements with the simultaneous coupling between the explicit and implicit terms.

In applying the semi-implicit method to Navier-Stokes equation (18), global Jacobian matrices J comes from the implicit method and can be defined by $\mathbf{J}(\mathbf{u}) = \partial\mathbf{g}/\partial\mathbf{u}$. As the derivations in Ref. [34], the fifth-order upwind scheme and sixth-order central scheme are used to approximate the derivatives of $\frac{\partial()}{\partial\eta}$ and $\frac{\partial^2()}{\partial\eta^2}$. This leads to

$$\begin{aligned} \delta\mathbf{g}(U_{ijk}) \;=\; & \mathbf{A}_{ijk}\delta U_{ij-3k} + \mathbf{B}_{ijk}\delta U_{ij-2k} + \mathbf{C}_{ijk}\delta U_{ij-1k} \\ & + \mathbf{D}_{ijk}\delta U_{ijk} + \mathbf{E}_{ijk}\delta U_{ij+1k} + \mathbf{F}_{ijk}\delta U_{ij+2k} \\ & + \mathbf{G}_{ijk}\delta U_{ij+3k} \end{aligned} \tag{20}$$

where the coefficient matrices can also be found in Ref. [34].

The final global Jacobian matrix for the system of ordinary differential equations, Eq. (18), is a block seven-diagonal matrix involving terms along the j grid direction only. This block seven-diagonal system of equations can be solved efficiently by a banded matrix solver.

The physical boundary conditions for viscous flows are non-slip condition for velocity and isothermal or adiabatic condition for temperature. The freestream flow conditions are specified by a given flow. For the flow disturbed by disturbances, the disturbances are specified according to the particular physical nature of the disturbances. Since the emphasis of current paper is the parallelized semi-implicit method for efficient and accurate time integration of the governing equations, we will mainly consider flows with a supersonic exit where the reflection of disturbances are negligible.

Boundary conditions on the wall are included in the global Jacobian matrix to ensure that it is a global implicit equation and advanced in time. For example, to include the lower wall boundary conditions, by imposing the fourth-order boundary conditions, δU_{i1k} can be written as,

$$\begin{aligned} \delta U_{i1k} \;=\; & (\frac{\partial U}{\partial V})_{i1k}(\frac{\partial V_{i1k}}{\partial V_{i2k}})(\frac{\partial V}{\partial U})_{i2k}\delta U_{i2k} \\ & + (\frac{\partial U}{\partial V})_{i1k}(\frac{\partial V_{i1k}}{\partial V_{i3k}})(\frac{\partial V}{\partial U})_{i3k}\delta U_{i3k} \\ & + (\frac{\partial U}{\partial V})_{i1k}(\frac{\partial V_{i4k}}{\partial V_{i4k}})(\frac{\partial V}{\partial U})_{i4k}\delta U_{i4k} \\ & + (\frac{\partial U}{\partial V})_{i5k}(\frac{\partial V_{i1k}}{\partial V_{i5k}})(\frac{\partial V}{\partial U})_{i5k}\delta U_{i5k} \end{aligned}$$

where $\frac{\partial V_{i1k}}{\partial V_{ijk}}(j = 2, ..., 5)$ is the coefficients of the corresponding boundary conditions applied to the lower wall.

2.2.2 Parallelization Approach

The standard(portable) message passing interface(MPI) is the parallel library we used to parallelize our code. A cluster of workstations are used to run our parallel codes. The present configuration has 14 RISC/6000 processors. The main memory capacity of these nodes is 256 megabytes. All of these nodes are connected via ethernet.

The first step of parallelization approaches is to initialize the MPI environment and to establish communicators that describe the communication contexts and the associated groups of processors. The MPI_COMM_WORLD default communication that defines one communication context and uses the set of all processors as its group is the one we used in this version. There are several modes of communication in MPI. In this work the data exchange at the block boundaries is implemented using the MPI_SENDRECV routine. This routine is a locally blocking one which means that a send or a receive would not return until it is complete, and therefore a tight synchronization is achieved among the processors. Divide and Conquer (DAC) method is implemented to solve the big banded Jacobian matrices of implicit algorithms during numerically solving high-order discretized nonlinear Navier-Stokes equations on massively distributed memory computers. Details of the method can be found in Ref. [30].

3 Numerical Results

A flexible three-dimensional solver has been written by using parallelized explicit and semi-implicit high-order upwind schemes for the spatial discretization with a high-order shock fitting algorithm. Fourier collocation method are used in computing the azimuthal direction. Our numerical codes have firstly been validated by simulating the the case of supersonic flow over a sphere. We then compare our numerical results with results predicted by LST by forcing a temporally periodical fluctuation into 2-D flow field. At last, we study the hypersonic boundary layer receptivities to fast acoustic wave and vorticity wave over 3-D blunt wedge. Investigations have been done as followings:

3.1 Supersonic Flow over a Sphere

As the first validation of the new parallel semi-implicit code, a sphere is chosen since there are a lot of experimental results for a sphere in supersonic flow [35,36]. Our numerical results are compared with exper-

imental results to check the accuracy of the new implicit parallel algorithms.

The body surface is a sphere given by:

$$x^{*2} + y^{*2} + z^{*2} = d^{*2} \tag{21}$$

where d^* is the radius of the sphere and is used as the reference length. The flow conditions are

$M_\infty = 5.25$ and 7.4 $\quad \epsilon = 5 \times 10^{-4}$
$T^*_\infty = 192.989\,K$ $\quad p^*_\infty = 10.3\,Pa$
$T^*_w = 1000\,K$ $\quad \gamma = 1.4$
$R^* = 286.94\,Nm/kgK$ $\quad Pr = 0.72$
$d^* = 0.6\,m$
$T^*_r = 288\,K$ $\quad T^*_s = 110.33\,K$
$\mu^* = 0.17894 \times 10^{-4} kg/ms$
$Re_\infty = \rho^*_\infty U^*_\infty d^*/\mu^*_\infty = 36,159.3$

The body surface is assumed to be a non-slip wall with an isothermal wall temperature T^*_w.

The results presented in here are obtained using 91 grid points in the streamwise direction and 61 points in the wall-normal direction. 32 Fourier collocation points are used in computing the azimuthal direction. 6 processors are using to run the high-order parallel implicit codes. Figure 2 shows the steady solution for a set of $90 \times 60 \times 32$ computational grids. Bow shocks are captured well by the methods. Figure 3 shows the computed and experimental pressure coefficients

$$c_p = \left(p_{\text{body}} - p_\infty\right) / (\gamma/2) p_\infty {M_\infty}^2 \tag{22}$$

for Mach number 5.25 and Mach number 7.4 in Cleary's experiments [36]. The agreement is pretty good, at least to within the scatter in the experimental data. Because of the way that the experiments were done, Cleary claimed that the data should only be accurate to $x' = 0.75$. We still can see good agreement for the larger values of x'. Figure 4 compares the computed and experimental bow shock shapes for two test cases with freestream Mach numbers of 2 and 4. Numerical results compare very well with the experimental results. Our numerical methods method can approach high-order accuracy in DNS of 3-D boundary layer problem.

3.2 Hypersonic Flow over 3-D Parabola Wedge

Our new 3-D parallel shock-fitting hypersonic DNS code has been applied to DNS of the receptivity of a three-dimensional boundary layer to weak freestream oblique acoustic disturbance waves for a hypersonic flow boundary layer over a 3-D parabolic leading edge whose body surface is given by

$$x^* = b^* {y^*}^2 - d^* \tag{23}$$

where b^* is a given constant and d^* taken as the reference length. The body surface is assumed to be a non-slip wall with an isothermal wall temperature T^*_w.

The specific flow conditions are

$M_\infty = 15$ $\quad \epsilon = 5 \times 10^{-4}$
$T^*_\infty = 192.989\,K$ $\quad p^*_\infty = 10.3\,Pa$
$T^*_w = 1000\,K$ $\quad \gamma = 1.4$
$R^* = 286.94\,Nm/kgK$ $\quad Pr = 0.72$
$T^*_r = 288\,K$ $\quad T^*_s = 110.33\,K$
$\mu^* = 0.17894 \times 10^{-4} kg/ms$

Low Reynolds number case:
$b^* = 40\,m^{-1}$ $\quad d^* = 0.1\,m$
Nose Radius of Curvature $= r^* = 0.0125\,m$
$Re_\infty = \rho^*_\infty U^*_\infty d^*/\mu^*_\infty = 6026.55$

High Reynolds number case:
$b^* = 4\,m^{-1}$ $\quad d^* = 1.0\,m$
Nose Radius of Curvature $= r^* = 0.125\,m$
$Re_\infty = \rho^*_\infty U^*_\infty d^*/\mu^*_\infty = 60265.5$

There is no flow in spanwise direction.

In the simulations, steady flow solutions are first obtained by advancing the unsteady flow computations to convergence using the new parallelized semi-implicit computer code. No disturbances are imposed in the freestream. The results presented in here are obtained by using 161 grid points in the streamwise direction and 121 points in the wall-normal direction, 4 Fourier collocation points are used in computing the azimuthal direction. Figure 5 shows the steady solution for a set of $161 \times 121 \times 4$ computational grids obtained by the simulation. Figure 6 shows steady flow solutions for temperature and pressure contours obtained by using 12 processors simultaneously. Edges in figure are the boundaries of subdomains.

Validation of LST Results

Before we start to do the numerical simulation of receptivity of 3-D hypersonic flow, another test case is investigated to validate the accuracy of our numerical method. Necessary linear stability (LST) analysis is carried out to obtain more clear knowledgement of the characteristics of the wave used in the simulation. The Reynolds number, Re, used in the calculations is based on the local length scale. A more standard length scale $\delta(s)$ is used to scale the wave numbers and frequencies. $\delta(s)$ is defined as

$$\delta = \sqrt{\frac{s\nu_e}{U_e}} \tag{24}$$

where s is the distance from the leading dege.

A common forcing frequency is enforced in DNS. This frequency is also enforced locally at each station in the linear stability analysis during the study. In the normal mode analysis for the linear disturbances, the fluctuations of flow quantities are assumed to be represented by harmonic waves of the following form:

$$[u', v', p', T', w']^T = \left[\hat{u}(y), \hat{v}(y), \hat{p}(y), \hat{T}(y), \hat{w}(y)\right]^T e^{i(\alpha x + \beta z - \omega t)} \tag{25}$$

where α and β are the wavenumbers in x and z directions respectively, and ω is the frequency of the disturbance waves. These parameters are in general complex numbers. The complex amplitude (eigen) function of a typical flow variable, say u, is $\hat{u}(y)$. In order to compare with the DNS results, spatially stability problem is solved. In a spatial stability problem, real-valued ω and β are assumed. While α is the complex eigenvalue to be solved for. The real part of α, α_r, represents the spatial frequency of the disturbance modes, while the imaginary part, α_i, represents the spatial amplification rate of the disturbances. When $-\alpha_i$ is greater, equal to, or smaller than zero, a disturbance mode is unstable with finite amplification, neutrally stable, or stable with finite damping, respectively. In our research, a range of forcing frequency is studied for obtaining spatial amplification rate of the disturbances.

The subsonic mode with fixed frequency $F = 1.9 \times 10^{-4}$ is introduced through the inflow condition located at $Re = 800$. Figure 7 shows the computational domain. The second mode is predicted unstable from $Re = 915$ to $Re = 987$ by LST at this fixed frequency. And it is found only the subsonic mode will transition to unstable. The unsteady computations are carried on till the solutions reach a periodic state. After that, unsteady computations are conducted for one period in time. Temporal Fourier analysis is performed on the results of the unsteady flow in one period to obtain amplitude and phase angle of disturbances as follows,

$$\phi'(x,y,t) = |\phi'| e^{i(\psi'(x,y)-\omega t)} \tag{26}$$

Streamwise wavenumber can be extrated from DNS by using

$$\alpha_r = \frac{d|\psi'|}{dx} \tag{27}$$

$$\alpha_i = -\frac{1}{|\phi'|}\frac{d|\phi'|}{dx} \tag{28}$$

We then can compare wave numbers and growth rates from numerical simulation are compared with the eigenvalues obtained from linear stability analysis based on the same mean flow.

Figure 8 is the comparison of real part of the p' eigen function of the unstable second mode obtained by using DNS and LST analysis at $Re = 947$ in the computational domain. The shape of this eigen function is close to Mack's work [11]. Figure 9 shows the comparison of streamwise wavenumbers and growth rates between the results from numerical simulation and LST respectively. In the figure, the real part and the imaginary parts of α are the wavenumbers and growth rates respectively. It shows that there is a good agreement between the results of simulation and LST on α_r and α_i.

Receptivity Simulations

The receptivity problems are studied numerically by solving the unsteady Navier-Stokes equations using a high-order parallelized semi-implicit method. There are two kinds of weak perturbation waves in a uniform flow studied in the freestream in this paper. They are fast acoustic waves, and vorticity waves. The perturbations of an arbitrary flow variables before reaching the bow shock can be written in the following form:

$$q'_\infty = |q'|_\infty e^{i(\mathbf{k}_\infty \hat{\mathbf{x}} - \omega \mathbf{t})} \tag{29}$$

where $|q'|$ represents one of the flow variables, $|u'|$, $|v'|$, $|w'|$, $|p'|$, and $|\rho'|$, $\mathbf{k}_\infty$ is the wavenumber, and ω is the wave frequency in the freestream before reaching the shock. The freestream perturbation amplitudes satisfy the following dispersion relations:

Fast Acoustic Waves($c^*_\infty = u^*_\infty + a^*_\infty$):

$$|u'|_\infty = \epsilon \cos\psi\,, \qquad |v'|_\infty = 0\,,$$
$$|p'|_\infty = \gamma M_\infty \epsilon\,, \qquad |\rho'|_\infty = M_\infty \epsilon$$
$$|w'|_\infty = \epsilon \sin\psi$$

where ϵ represents the freestream wave magnitude. The angle ψ is the angle of freestream wave with respect to the x axis in the x-z plane, where $\psi = 0$ corresponds to 2-D planar fast acoustic waves.

Vorticity Waves($c^*_\infty = u^*_\infty$):

$$|v'|_\infty = \epsilon \cos\psi\,, \qquad |u'|_\infty = 0\,,$$
$$|p'|_\infty = 0\,, \qquad |s'|_\infty = 0$$
$$|w'|_\infty = \epsilon \sin\psi$$

where the angle ψ is the angle of freestream wave with respect to the y axis in the y-z plane for vorticity waves. The parameter k is the dimensionless freestream wave number which is related to the dimensionless circular frequency ω by:

$$\omega = k\,(\cos\psi + M_\infty^{-1}) \tag{30}$$

The dimensionless frequency F is defined as:

$$F = \frac{\omega^* \nu^*}{U^{*2}_\infty}\,. \tag{31}$$

After we obtained good steady mean flow of hypersonic flow over blunt wedge, unsteady viscous flows are computed by imposing a continuous planar acoustic single-frequency wave or vorticity wave on the steady flow variables at the free stream side of the bow shock. The unsteady simulation is nonlinear by computing the transient flow solutions of the Navier-Stokes equations without any linearization in the equations and in the shock jump conditions. The wave interaction with the shock and the development of instability wave in the boundary layer are simultaneously resolved by the simulation. The unsteady calculations are carried out for about 20 to 40 temporal periods until the solutions reach a periodic state in time. Then, the unsteady computations are carried out for one additional period in time to record the perturbations with respect to the steady flow field obtained previously. A fast Fourier

transform (FFT) is performed on the perturbation variables to obtain the Fourier amplitudes and phase angles of the perturbations of the unsteady flow variables throughout the flow field.

Receptivity to Fast Acoustic Waves

The generation of boundary-layer T-S and inviscid instability waves by freestream acoustic disturbances for hypersonic flow over 3-D parabolic leading edge has been firstly simulated by studied the cases of introducing single oblique wave, and introducing two oblique waves into the steady mean flow, For two oblique acoustic waves, we present the results of two 45^0 acoustic waves here. For single oblique acoustic waves, we change the freestream disturbance wave angle ψ from 0^0 to 15^0, 30^0, 45^0, 55^0, 60^0.

Figure 10 shows the 3-D contours of the instantaneous perturbation u' the streamwise velocity for single $\psi = 45^0$ oblique wave case at $F = 1770$. Figure 11 shows contours of the instantaneous perturbation velocity, u', and the Fourier amplitude $\mid u' \mid$ after the flow field has reached a periodic state. Figure 12 shows the 3-D contours of the instantaneous perturbation u' the streamwise velocity for two $\psi = 45^0$ oblique waves case at $F = 1770$. Figure 13 shows contours of the instantaneous perturbation u' and the Fourier amplitude $\mid u' \mid$. Both amplitude contours show a strong growth near the leading edge in the boundary layer on the wall, followed by a rapid decay and transition to another wave mode. These figures show two distinct main wave zones of first and second mode instability waves. The first mode is much stronger than the second mode for the current test case. From the figure, the characteristics of the switching of instability modes for first mode instability dominated region to second mode with the sudden phase angle change near the body surface around $x = 0.1$ can be observed. Figure 14 shows the comparison of distribution of the maximum amplitude of streamwise velocity between the single oblique acoustic wave case and the case of two oblique waves. The single oblique acoustic wave performs higher growth than the case of two oblique waves. We then stick on the case of single oblique acoustic wave to do further studies.

We enforce the same wave number k, and compare the velocity Fourier amplitudes by changing angle ψ to 0^0 to 15^0, 30^0, 45^0, 55^0, 60^0 for single oblique acoustic wave case. Figure 15 shows the comparison of distribution of the Fourier amplitude $\mid u' \mid$ along x axis. Figure 16 shows the comparison of the maximum Fourier amplitude $\mid u' \mid$ of the first mode. For the first mode, the maximum Fourier amplitude occurs around $\psi = 45°$. But for the second mode, the maximum Fourier amplitude occurs on the 2-D wave case of $\psi = 0°$. This is same as the conclusion of Mach's work [11], where the 3-D effects on linear stability of compressible flat plate boundary layer were studied.

A number of computational cases are studied on the effects of frequency, and the effects of the freestream disturbance wave angle on the hypersonic receptivity process. Seven different cases with different frequencies are tested by numerical simulations as followings.

Table 1: **Seven Different Frequencies**

Case Number	F
A.1	2655
A.2	2212.5
A.3	1770
A.4	1327.5
A.5	1008.9
A.6	769.95
A.7	531

By fixing above frequencies, three different the freestream disturbance wave angles are studied. They are 0^0, 45^0, and 85^0. To study to the effects of wave angles and the effects of disturbance frequency, we are mainly study the effects to amplitude of the first-mode wave. Figure 17 shows the comparisons of the distributions of maximum Fourier amplitude $\mid u' \mid$ for $\psi = 0°, 45°, 85°$ at the same frequency $F = 1770$. For this figure, we can find the Fourier amplitude of $\mid u' \mid$ has a stronger growth near the leading edge at $\psi = 85°$ than the growth of $\psi = 0°$ case due to the 3-D effect. For $\psi = 85°$ case, even the 3-D effect is strong, however, at such high frequency, there is no strong growth can be observed. Figure 18 shows the comparisons of the spectrum of maximum Fourier amplitude $\mid T' \mid$ for $\psi = 0°, 45°, 85°$ at different frequency. Along with the decreasing of frequency, the maximum Fourier amplitude $\mid T' \mid$ is increasing. But the growth can not reach very high value due to acoustic wave receptivities. However, even the transient growth is not that strong, we still can observe the big growth near the leading edge.

Receptivity to Vorticity Waves(On-going)

According to Ref. [25], streamwise vortices is a very reasonable means of exciting transient growth. To approach much stronger growth of the disturbances near the leading edge, we are studying the vorticity wave receptivities of low Reynolds number base flow and high Reynolds number base flow. The results represented here are the results of low Reynolds number flow only. For vorticity waves, in the freestream, nonzero disturbances are normal and spanwise velocity disturbances(v' and w') and wavenumber (k_y and k_z). Amplitudes of other disturbances are zero. The results represented here are only the cases of $\psi = 30^0$ in the low Reynolds number base flow. Unlike acoustic waves, vorticity waves are hard to entry the boundary layer.

In this paper, two different heights of vorticity wave beams, 0.1m and 0.03m, are tested. On the other hand, we also compare the results of vorticity wave receptivities of two different streamwise wavenumber cases. One is the case of zero streamwise wavenumber which gives zero wave frequency. The other is the non-zero streamwise wavenumber case.

Figure 19 shows the 3-D and 2-D streamwise velocity perturbation contours of first two computational zones near the leading edge for the case with 0.1m height of vorticity beam and zero streamwise wavenumber. The figure shows that freestream vorticity waves enter the computational computational domain at top boundary. The figure also shows that vorticity layer also exist inside boundary layer which is induced by vorticity waves entered near the leading edge. Figure 20 shows the streamwise velocity perturbation distribution and disturbance energy distribution inside the boundary layer. We can find that there is a large growth near the leading edge due to the introducing of vorticity wave. For the energy density plot, the strength of energy approaches the maximum at the location of -0.7.

Figure 21 shows the 3-D streamwise velocity perturbation contours of first two computational zones near the leading edge for the case with 0.03m height of vorticity beam and zero streamwise wavenumber. Figure 22 is the 2-D cross-secion of above streamwise velocity perturbation contour. From Figure 23, the disturbance performs stronger growth and higher value of disturbance energy than the height of 0.1m case. This is because the peak of vorticity wave is much closer to the leading edge which leads earlier entrance to the boundary layer. To obtain enough growth of disturbance excited by vorticity wave, more test cases will be completed in the future computations.

Figure 24 shows the 3-D and 2-D streamwise velocity perturbation contours of the case with 0.03m height of vorticity beam and non-zero streamwise wavenumber. By introducing ω, disturbances become temporally periodic. From Figure 25, the disturbance has higher value of disturbance energy than zero streamwise wavenumber case. Figure 26 shows the amplitude of streamwise velocity perturbation in one cross-section of the flow field. Besides the disturbance very close to the leading edge, there is another mode excited by the vorticity wave. More detailed numerical simulations will be continued to find the optimal combination of frequency and Reynolds numbers which will lead maximum growth.

4 Summary and Future work

High-order parallelized computer codes which include parallel Fourier spectral method have been implemented to do the direct simulations of fully 3-D hypersonic boundary layers over a blunt body to freestream fast acoustic disturbances and vorticity disturbances using 3-D unsteady Navier-Stokes equations. Validation cases show that our numerical methods are high accurate for the simulations of compressible flow over blunt bodies. The receptivity results show a strong growth near the leading edge in the boundary layer on the wall. Due to 3-D effect, acoustic wave receptivity performs larger growth than 2-D case. On the cases of vorticity wave receptivities, after vorticity wave entering boundary layer, high growth of disturbance is observed. By coupling the streamwise disturbance, large growth appears. A set of computational cases including a full spectrum of streamwise frequencies and high Reynolds number case will be completed soon.

Acknowledgments

This work was sponsored by the Air Force Office of Scientific Research, USAF, under AFOSR Grant # F49620-00-1-0101 monitored by Dr. John Schmisseur. The views and conclusions contained herein are those of the author and should not be interpreted as necessarily representing the official policies or endorsements either expressed or implied, of the Air Force Office of Scientific Research or the U.S. Government.

References

[1] Morkovin, M. V. and Reshotko, E., "Dialogue on Progress and Issues in Stability and Transition Research," *In Laminar-Turbulent Transition, IUTAM Symposium, Toulouse, France, 1989, D. Arnal, R. Michel, Editors*, Vol. Springer-Verlag Berlin, 1990.

[2] Herbert, T., "Progress in Applied Transition Analysis," *AIAA paper 96-1993*, 1996.

[3] Bushnell, D., "Notes on Initial Disturbance Field for the Transition Problem," *Instability and Transition, Vol. I*, Vol. M. Y. Hussaini and R. G. Viogt, editors, pp. 217-232, Springer-Verlag, 1990.

[4] Morkovin, M., "On the Many Faces of Transition," *Viscous Drag Reduction*, C.S. Wells, editor, Plenum 1969.

[5] Goldstein, M. E., "The evolution of Tollmien-Schlichting Waves near a Leading Edge," *Journal of Fluid Mechanics*, Vol. 127, pp. 59-81 1983.

[6] Kerschen, E. J., "Boundary-Layer Receptivity," *AIAA paper 89-1109*, 1989.

[7] Murdock, J. W., "Tollmien-Schlichting Waves Generated by Unsteady Flow over Parabolic Cylinders," *AIAA paper 81-0199*, 1981.

[8] Lin, N., Reed, H. L., and Saric, W. S., "Effect of Leading-Edge Geometry on Boundary-Layer Receptivity to Freestream Sound," *Instability, Transition, and Turbulence*, M. Y. Hussaini et al., editors, pp. 421-440, Springer-Verlag 1992.

[9] Buter, T. A. and Reed, H. L., "Boundary layer receptivity to free-stream vorticity," *Physics of Fluids*, Vol. 6, No. 10, 1994, pp. 3368–3379.

[10] Collis, S. S. and Lele, S. K., "A Computational Approach to Swept Leading-Edge Receptivity," *AIAA paper 96-0180*, 1996.

[11] Mack, L. M., "Boundary Layer Linear Stability Theory," AGARD report, No. 709, 1984.

[12] Morkovin, M. V., "Transition at Hypersonic Speeds," *ICASE Interim Report 1*, NASA CR 178315, May 1987.

[13] Arnal, D., "Laminar-Turbulent Transition Problems In Supersonic and Hypersonic Flows," *Special Course on Aerothermodynamics of Hypersonic Vehicles*, AGARD Report No. 761 1988.

[14] Reed, H. L. and Saric, W. S., "Stability of Three-Dimensional Boundary Layers," *Annual Review of Fluid Mechanics*, Vol. 21, pp. 235-284, 1989.

[15] Reshotko, E., "Hypersonic Stability and Transition," *in Hypersonic Flows for Reentry Problems, Eds. J.-A. Desideri, R. Glowinski, and J. Periaux, Springer-Verlag*, Vol. 1, 1991, pp. 18–34.

[16] Kovasznay, L. S. G., "Turbulence in Supersonic Flow," *Journal of the Aeronautical Sciences*, Vol. 20, No. 10, October 1953, pp. 657–682.

[17] Mckenzie, J. F. and Westphal, K. O., "Interaction of Linear Waves with Oblique Shock Waves," *The Physics of Fluids*, Vol. 11, No. 11, November 1968, pp. 2350–2362.

[18] Saric, W. S., "Götler Vortices," *Annual Review of Fluid Mechanics*, Vol. 26, pp. 379-409, 1994.

[19] Landahl, M. T., "A note on an Algebraic Instability of Inviscid Parallel Shear Flows," *Journal of Fluid Mechanics*, Vol. 98, part 2, pp. 243-251, 1980.

[20] Butler, K. M. and Farrell, B. F., "Three-Dimensional Optimal Perturbations in Viscous Shear Flow," *Physics of Fluid*, Vol. 4, No. 8, pp. 1637-1650, 1992.

[21] Breuer, K. S. and Kuraishi, T., "Transient Growth in Two- and Three-dimensional Boundary Layers ," *Physics of Fluids*, Vol. 6, No. 6, June 1994.

[22] A. Hanifi, P. J. S. and Henningson, D. S., "Transient Growth in Compressible Boundary Layer Flow," *Physics of Fluids*, Vol. 8, No. 3, March 1996.

[23] P. Andersson, M. B. and Henningson, D. S., "Optimal Disturbances and Bypass Transition in Boundary Layers ," *Physics of Fluids*, Vol. 11, No. 1, January 1999.

[24] Reshotko, E. and Tumin, A., "Spatial Theory of Optimal Disturbances in a Circular Pipe Flow ," *Physics of Fluids*, Vol. 13, No. 4, April 2001.

[25] Reshotko, E., "Transient Growth: A Factor in Bypass Transition," *Physics of Fluids*, Vol 13, No. 5, pp. 1067-1075 May 2001.

[26] M. V. Morkovin, E. R. and Herbert, T., "Transition in Open Flow Systems - A Reassessment," *Bull. Am. Phys. Soc.*, 39, 1882, 1994.

[27] Tumin, A. and Reshotko, E., "Spatial Theory of Optimal Disturbances in Boundary Layers," *Physics of Fluids*, Vol. 13, No. 7, July 2001.

[28] Zhong, X., "High-Order Finite-Difference Schemes for Numerical Simulation of Hypersonic Boundary Layer Transiton," *Journal of Computational Physics*, Vol. 144, August 1998, pp. 662-709.

[29] Dong, H. and Zhong, X., "High-Order Semi-Implicit Schemes for Unsteady Compressible Flow Simulations," *AIAA Journal*, Vol. 40, No. 5, 2002.

[30] Dong, H. and Zhong, X., "A Parallel High-Order Implicit Algorithm for Compressible Navier-Stokes Equations," *AIAA paper 2000-0275*, January 2000.

[31] Zhong, X., "Direct Numerical Simulation of Hypersonic Boundary-Layer Transition Over Blunt Leading Edges, Part I: New Numerical Methods and Validation ," AIAA paper 97-0755, Jan. 1997.

[32] Zhong, X., "Additive Semi-Implicit Runge-Kutta Schemes for Computing High-Speed Nonequilibrium Reactive Flows," *Journal of Computational Physics*, Vol. 128, 1996, pp. 19-31.

[33] Yoh, J. J. and Zhong, X., "Low-Storage Semi-Implicit Runge-Kutta Methods for Reactive Flow Computations," AIAA paper 98-0130, Jan. 1998.

[34] Dong, H. and Zhong, X., "High-Order Semi-Implicit Simulation of Hypersonic Boundary Layer Stability and Transition," *AIAA paper 98-0127, 36th AIAA Aerospace Sciences Meeting and Exhibit, January 12-15, Reno, Nevada*, 1998.

[35] Kopriva, D. A., "Multidomain Spectral Solutions of High-Speed Flows over Blunt Cones," *AIAA Journal*, Vol. 31, No. 12, 1993.

[36] Cleary, J. W., "An Experimental and Theoretical Investigation of the Pressure Distribution and Flowfields of Blunted Cones at Hypersonic Mach Numbers," NASA TN D-2969 1965.

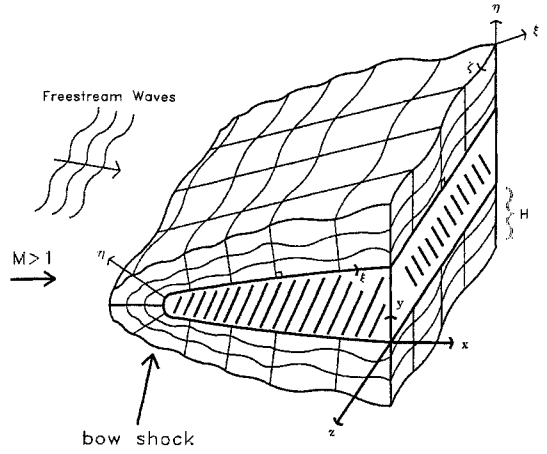

Figure 1: A schematic of 3-D shock fitted grids for the direct numerical simulation of hypersonic boundary-layer receptivity to freestream disturbances over a blunt leading edge.

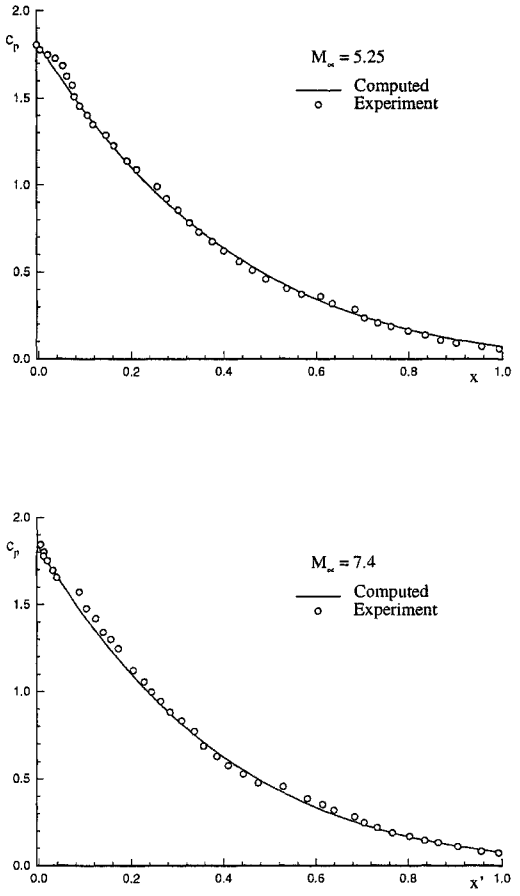

Figure 3: Comparison of pressure coefficients on a spherical body with different Mach numbers.

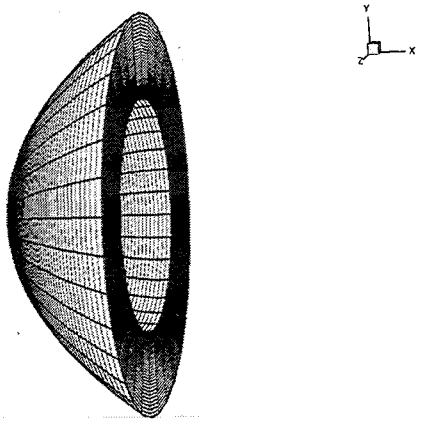

Figure 2: Steady flow solutions for $M_\infty = 5.25$ flow over a sphere by using high order 3-D shock-fitting method for computational grids where the bow shock shape is obtained as the freestream grid line.

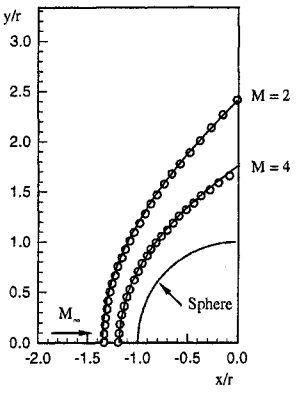

Figure 4: Bow shock locations for hypersonic flow over a sphere (lines: Numerical solutions, circles: experimental results).

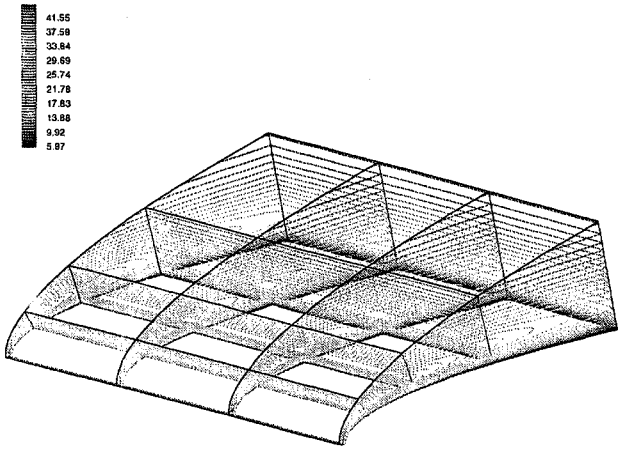

Figure 5: Steady flow solution of temperature contours for hypersonic flow over a blunt wedge by using high order parallelized code.

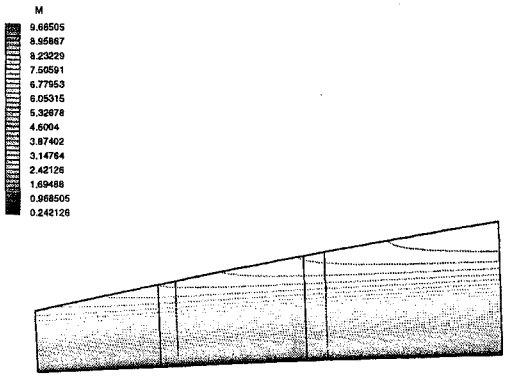

Figure 7: M contour of steady flow for 2-D enforcing mode case.

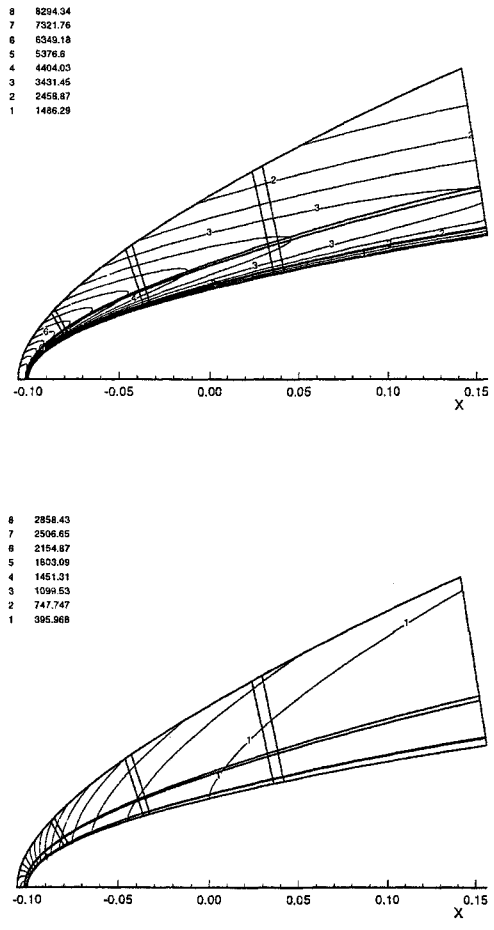

Figure 6: Steady flow solutions for hypersonic flow over a blunt wedge by using high order parallelized code for temperature (upper figure) and pressure contours (lower figure). Edges show the boundaries of each subdomain.

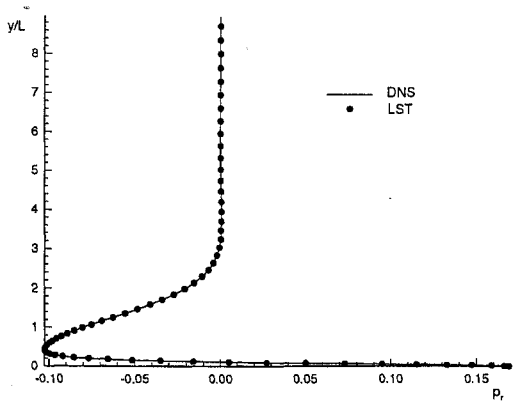

Figure 8: Comparison of eigenfunctions of pressure real part of the unstable second method obtained from DNS and LST.

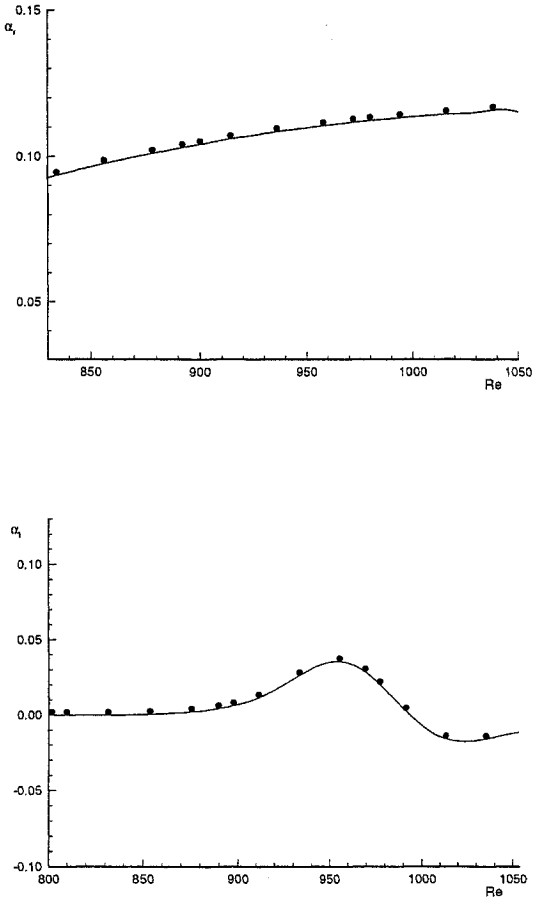

Figure 9: Comparison of streamwise wavenumber and growth rates between simulation (solid line) and LST calculation (dots).

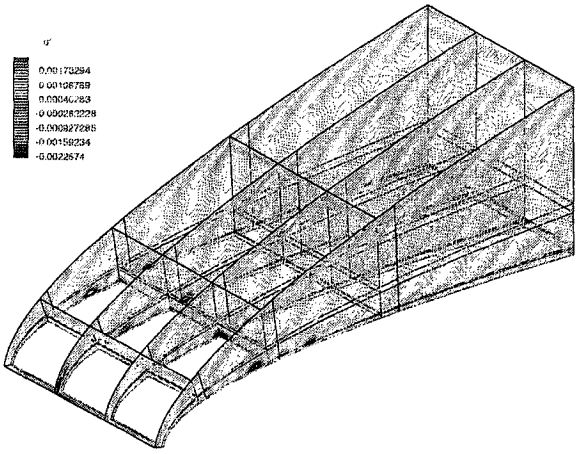

Figure 10: Instantaneous u' contours for the receptivity to freestream disturbances for 3-D hypersonic boundary-layer over a parabolic leading edge ($\psi = 45^0$). Edges show the boundaries of each subdomain.

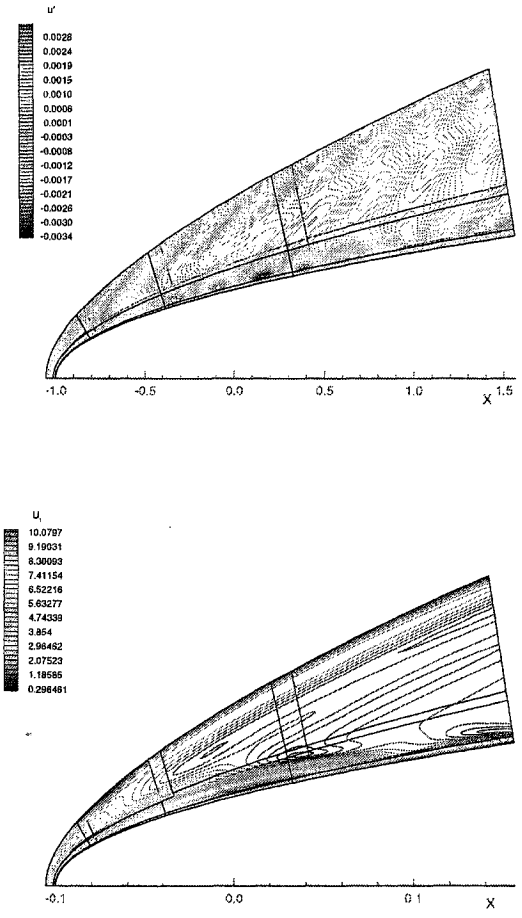

Figure 11: Instantaneous u' contours for the receptivity to single acoustic wave for 3-D hypersonic boundary-layer over a parabolic leading edge (upper figure) and Fourier amplitude $\mid u' \mid$ (lower figure)

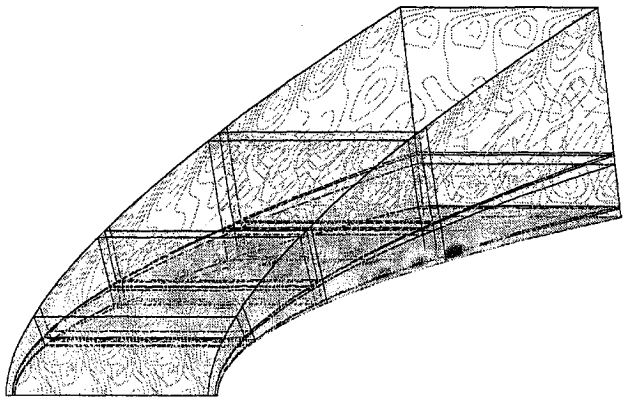

Figure 12: Instantaneous u' contours for the receptivity to two $\psi = 45^0$ oblique acoustic waves for 3-D hypersonic boundary-layer over a parabolic leading edge.

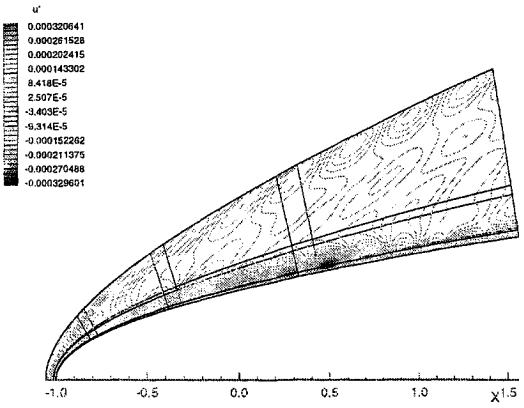

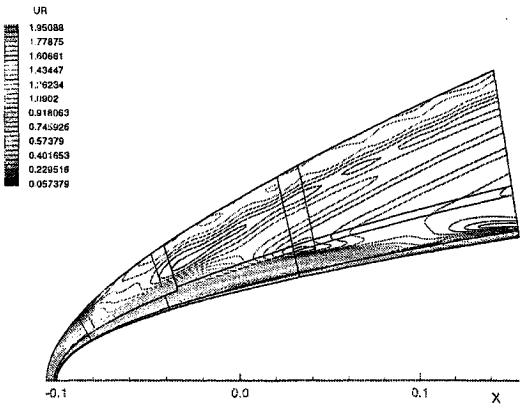

Figure 13: Instantaneous u' contours for the receptivity to two 45^0 oblique acoustic waves for 3-D hypersonic boundary-layer over a parabolic leading edge (upper figure) and Fourier amplitude $\mid u' \mid$ (lower figure)

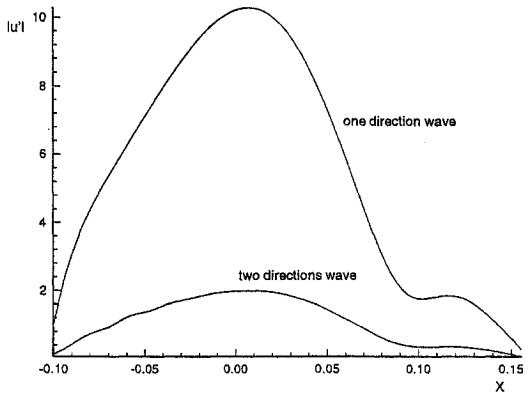

Figure 14: Comparison of the Fourier amplitude distributions between the case of single oblique wave and the case of two oblique waves.

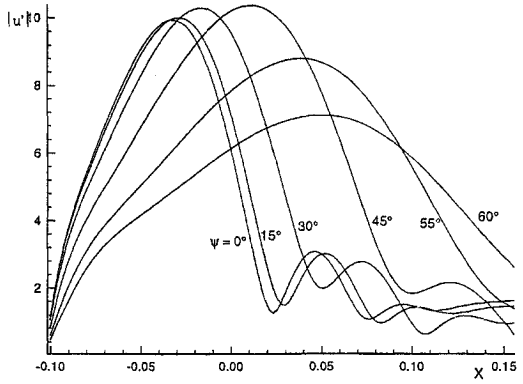

Figure 15: Comparison of the distribution of Fourier amplitude $\mid u' \mid$ along x axis for different ψ cases with same wavenumber.

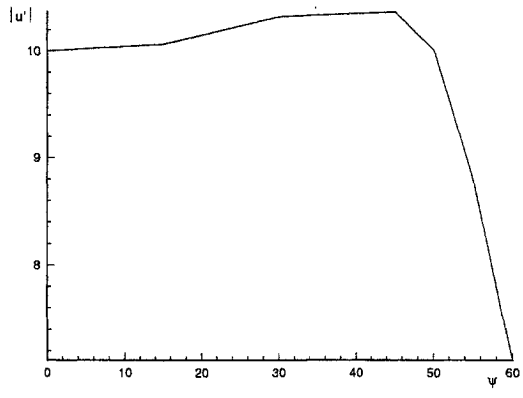

Figure 16: Comparison of maximum Fourier amplitude $\mid u' \mid$ for different ψ cases at fixed wavenumber.

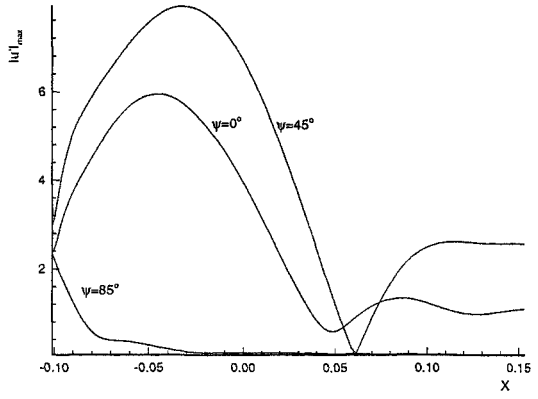

Figure 17: Comparison of distribution of maximum $|u'|$ for different ψ at fixed frequency.

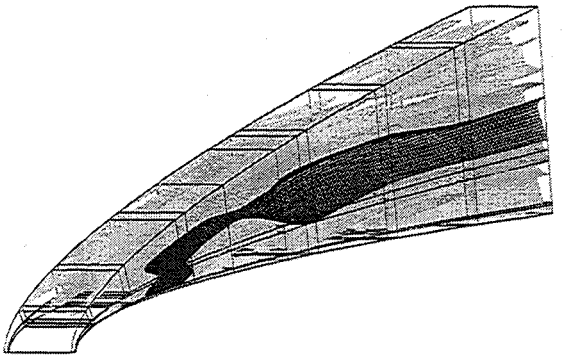

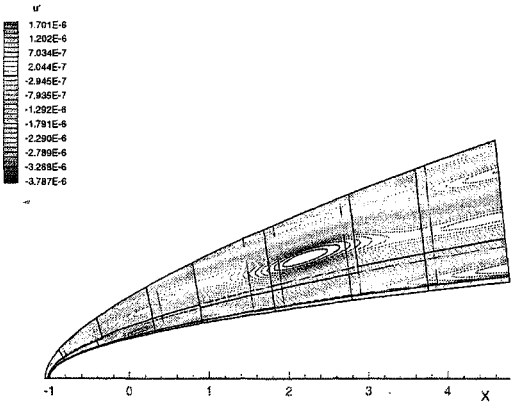

Figure 19: Streamwise velocity perturbation contours with 0.5m height of vorticity beam and zero streamwise wavenumber.

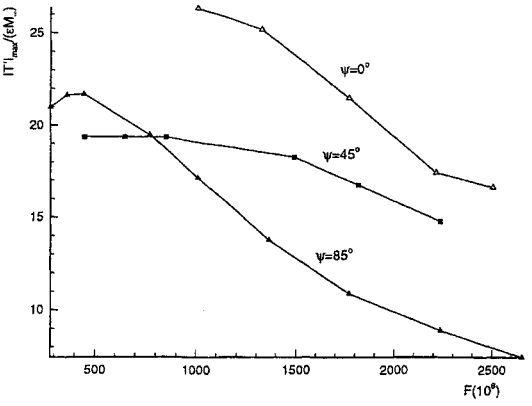

Figure 18: Comparison of maximum $|T'|$ along with the changing of frequencies for different ψ.

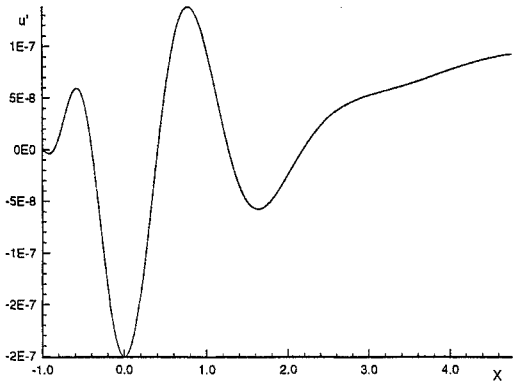

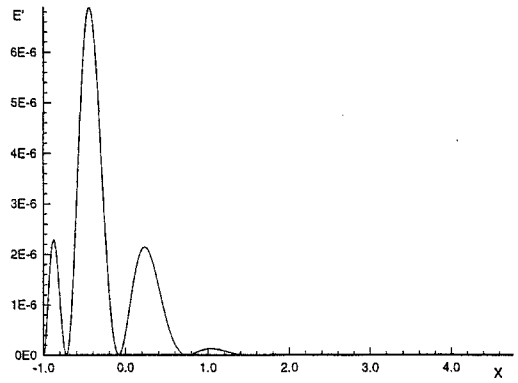

Figure 20: Streamwise velocity perturbation distribution and disturbance energy distribution for the case of 0.5m height of vorticity beam and zero streamwise wavenumber.

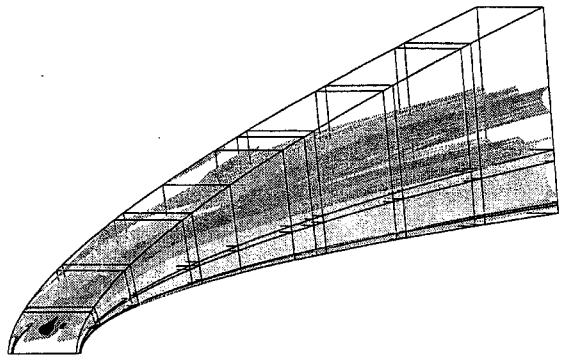

Figure 21: Streamwise velocity perturbation contour with 0.1m height of vorticity beam and zero streamwise wavenumber.

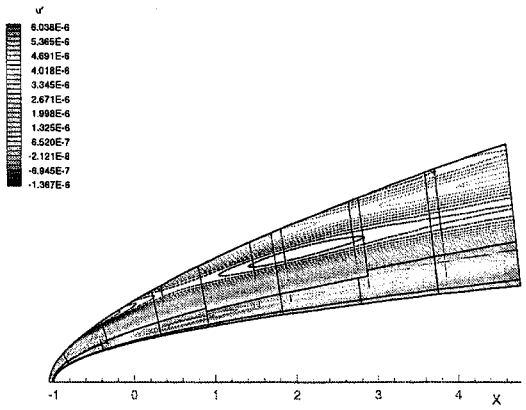

Figure 22: 2-D Streamwise velocity perturbation contour with 0.03m height of vorticity beam and zero streamwise wavenumber.

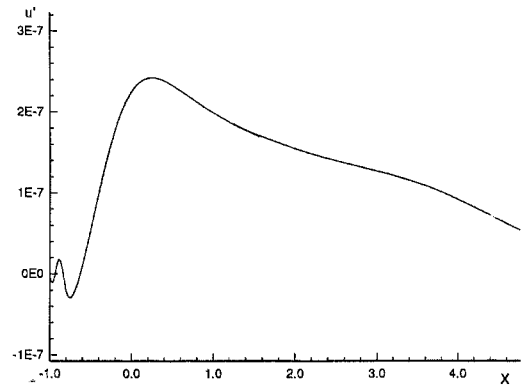

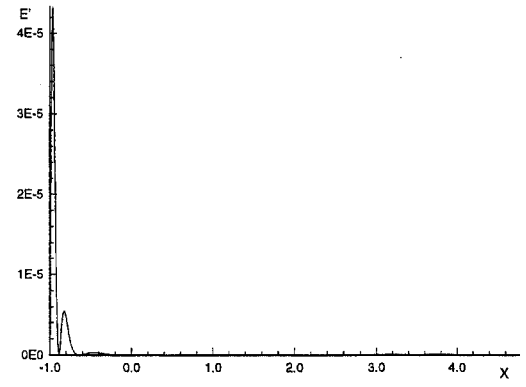

Figure 23: Streamwise velocity perturbation distribution and disturbance energy distribution for the case of 0.03m height of vorticity beam and zero streamwise wavenumber.

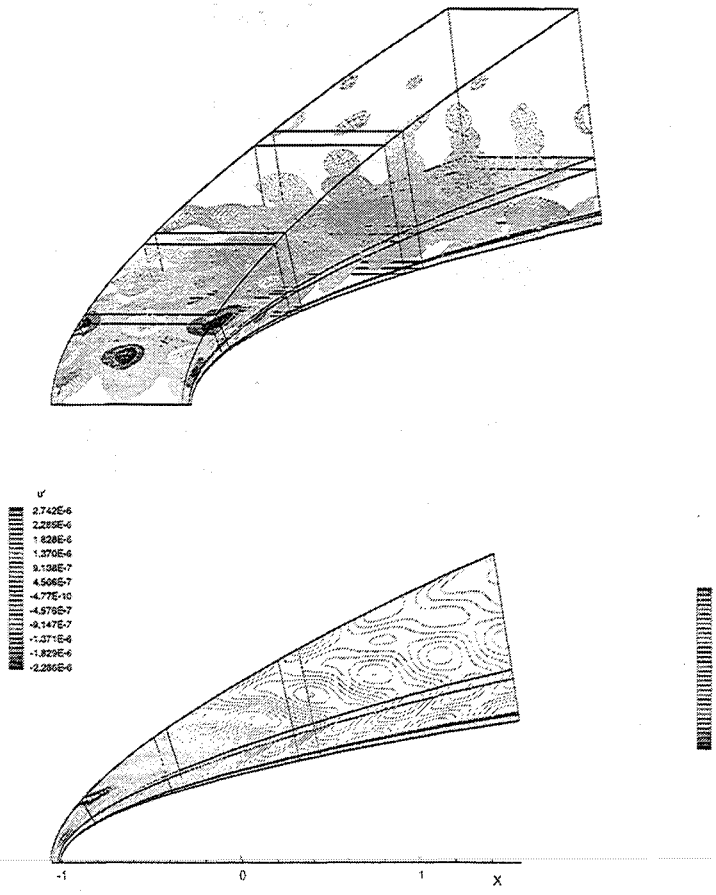

Figure 24: Streamwise velocity perturbation contours with 0.03m height of vorticity beam and non-zero streamwise wavenumber.

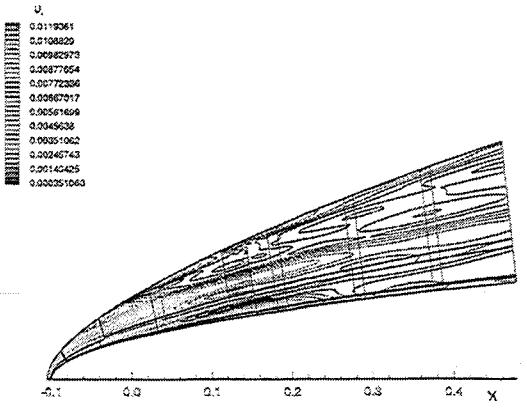

Figure 26: Amplitude of streamwise velocity perturbation for the case of non-zero streamwise frequency.

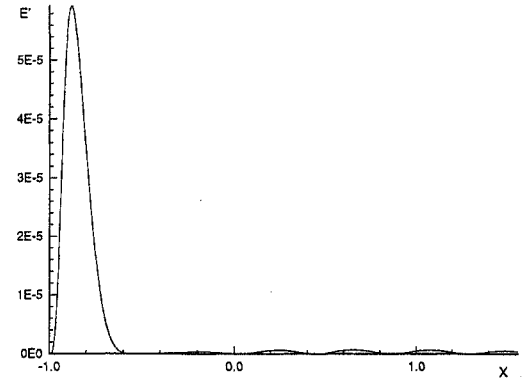

Figure 25: Streamwise velocity perturbation energy distribution for the case of 0.1m height vorticity wave beam and non-zero streamwise frequency.